An advanced structural trailing edge modelling method for wind turbine blades

Haselbach, Philipp Ulrich

Published in:
Composite Structures

Link to article, DOI:
10.1016/j.compstruct.2017.08.029

Publication date:
2017

Document Version
Early version, also known as pre-print

An Advanced Structural Trailing Edge Modelling Method For Wind Turbine Blades

Philipp Ulrich Haselbach[1,*]

Technical University of Denmark, Department of Wind Energy

Abstract

This study demonstrates an advanced blade modelling approach based on a combination of shell and solid elements which can enhance the reliability of structural predictions for wind turbine blades. The advanced blade modelling approach is based on a shell element model where the adhesive bondline in the trailing edge region is discretised by means of solid brick elements which are connected via Multi-Point-Constraint to the shell elements. The new approach overcomes the drawbacks of pure shell element simulations and can reliably predict the response of wind turbine blade structures which are exposed to ultimate loads. The prediction accuracy of the numerical simulations was compared to a certification load case and a full-scale ultimate limit state test of a 34m wind turbine rotor blade. The displacements, stresses and strains show reasonably good agreement and demonstrate the capabilities of the advanced blade modelling approach.

Keywords: Trailing edge modelling, buckling, shell elements, wind turbine rotor blade structure

1. Introduction

Blade design is an iterative process where several iterations loops are usually needed to define an optimal compromise between aerofoil geometry, structural design and aeroelastic response. An essential part of the design process for wind turbine blades is the use of *Finite Element Analyses* (FEA). Various different FEA specifically developed for wind turbine blades are usually conducted to optimise the aerodynamic, aeroelastic and structural behaviour, as well as the manufacturing processes.

Most of the published literature uses either beam model approaches or three-dimensional (3D) FEA based approaches to predict the structural response of wind turbine rotor blades. In theory, detailed 3D FEA based on solid brick elements reach the highest prediction accuracy, but come with high computationally costs and, therefore, are rarely used.

*Philipp Ulrich Haselbach
Email address: phih@dtu.dk (Philipp Ulrich Haselbach)
URL: http://www.vindenergi.dtu.dk/ (Philipp Ulrich Haselbach)
[1]DTU Wind Energy, Frederiksborgvej 399, DK-4000 Roskilde

To save computational time during the structural design and optimisation processes, computational efficient linear beam cross section analysis codes or linear beam element models are often used to predict the strain and stress state [1]. Beam cross sectional analysis codes, e.g. BECAS [2], predict the strain and stress state of single cross sections along the blade span. The advantage, apart of the computational efficiency of such linear cross sectional analyses, is that they define an interface plane, which allows the superposition of the acting forces (F_x, F_y, F_z) and moments (M_x, M_y and M_z) which are usually provided by aeroelastic load calculations [3]. Thus, detailed strain and stress states can be predicted for each cross section based on the load components by defining the boundary conditions. The disadvantage of linear beam element models and beam cross sectional analysis tools are that they neither account for geometrically non-linear deformations, such as cross-section ovalisation [4, 5, 6], nor are they able to predict stability problems (e.g. buckling). Moreover, beam models can only predict accurate 3D fields away from beam boundaries, concentrated loads and suddden changes in the cross-sectional geometry along the span, as commented by Chen et al. [1] in an assessment of computer tools for calculating composite wind turbine blade properties.

However, to reveal realistic failure mechanism and failure modes of the highly non-linear response of rotor blades, geometrically non-linear analyses are important [7]. Moreover, stability analyses are an essential part of the ultimate strength assessment of wind turbine blades, since buckling can be a failure mode [8, 6]. The ultimate limit state of wind turbine rotor blades depends heavily on local cross-sectional deformation, which is a highly non-linear phenomenon and varies depending on the load configurations [9, 8, 6, 10, 11]. Cross-section deformations are often provoked by combined load situations, where, for example, bending moments and torsional moments act simultaneously and need detailed and accurate prediction models able to handle these challenges. Therefore, the predictions based on simplified cross sectional analysis or beam models are only suitable for the first iteration steps, but not for the final ultimate limit state analysis of a wind turbine blade.

Detailed finite element analyses are usually performed to accurately predict the hollow and, to some extend, thin walled shell structures with a highly complex geometry of wind turbine rotor blades [9]. The FEA models usually consists of solid brick elements or shell elements. Modelling wind turbine rotor blades based on solid brick elements requires a very detailed geometry, since even layered solid elements require exact geometric thickness definition. Furthermore, the detailed geometric shape has to be discretised with a fine mesh in order to get an adequate accuracy [12]. The high mesh resolution usually makes the simulations computationally expensive and less attractive for running several iteration steps or analyses with different loadings.

Instead of FEA based solid brick elements less computationally expensive shell element approaches are usally used (see Cox and Echtermeyer [13]). Layered shell elements are computationally more efficient and do not require the same level of detail during the design phase. Moreover, the shell element formulation predicts the transverse shear stress through the thickness more accurately than a single row of layered solid brick elements does since the transverse shear stresses in solid elements do not usually vanish at the free surfaces of the structure and are usually discontinuous at layer interfaces. The transverse shear stresses in

thick shell elements are usually calculated on the basis of linear elasticity theory; such stresses are often better estimated by thick shell elements than by solid elements [14]. A drawback of wind turbine rotor blade shell element models can be that they do not represent the actual blade stiffness in the trailing edge region with the adequate accuracy as, for example, solid brick elements can do. Usually, shell element models predict a too low stiffness of the trailing edge region, since the joints in shell element models do not account for additional stiffness in regions where two shell elements intersect with overlapping material in thickness direction (shell normal).

This study demonstrates that an advanced blade modelling approach can overcome the drawbacks of shell element simulations and compares the accuracy of the numerical model with full-scale wind turbine rotor blade experiments. A 34 m wind turbine rotor blade is used to demonstrate an advanced blade modelling approach where the shell elements are combined with solid elements to improve the prediction quality. Moreover, two other modelling approaches are introduced and tested. Here, two shell element models with and without a tied trailing edge configuration are simulated and the predicted structural responses are investigated.

2. Method

For the numerical study, a finite element model of a 34 m wind turbine rotor blade was created. The model corresponds to the real blade structure, which consists of a box girder as the main load carrying structure surrounded by adhesively connected upper and lower panels which form the aerodynamic surface. The panels, forming the pressure-side and suction-side, are themselves connected by a trailing-edge joint and a leading-edge joint.

For the structural analysis of the blade, a numerical model created in Abaqus 6.14 was used. The initial geometry of the blade was discretised by $9.4x10^4$ 8-node doubly curved thick shell elements with reduced integration (Abaqus type S8R) with a characteristic element length of 0.05 m. The shell element thickness for the laminated (layered) shell elements was specified according to the composite material layup. The aerodynamic blade profile was chosen as the reference surface with an offset from the shell's midsurface which corresponded to half the material thickness to account for a continuously varying thickness of the layup. This means that the shell normal points from the reference surface towards the inner of the blade. The order of the laminated shell layers is aligned with the positive direction of the shell normal. The advantage of using the aerodynamic surface as the reference surface is that it represents the physical geometry more accurately [15]. No offset was chosen for the shear webs, where the geometrical middle of the shear webs was taken as the reference surface. Laminate layup and material properties were assigned to the layered shell elements. Three shell integration points for each layer were specified (Figure 1). The elastic material properties of the laminate layup components, as well as the properties of the epoxy based adhesive, are listed in Table 1. The indices 1 and 2 refer to the 0° and 90° direction respectively; E_{ij} represents the elastic modulus, G_{ij} represents the shear modulus, ν_{ij} denotes the Poisson's ratio, *Triaxial* is a triaxial glass fibre and *Triaxial 2* is a triaxial glass fibre with high resin content. *UD* represents unidirection glass fibre cloths, *Biaxial Pre* represents a

biaxial glass fibre pre-preg cloths, whereas *Biaxial* is a sprint biaxial glass fibre cloth and *Adhesive* represents the epoxy-based bonding paste used for the joints.

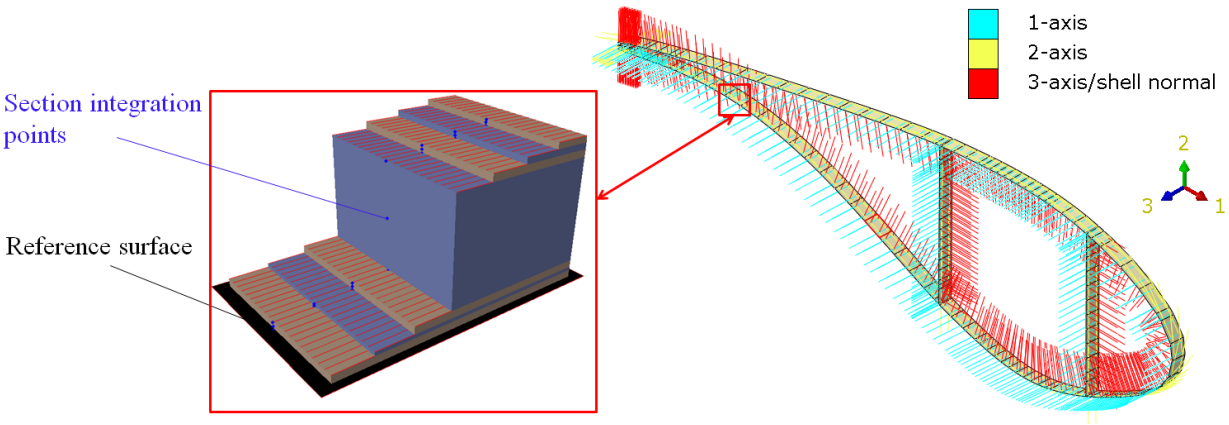

Figure 1: Material orientation of the blade model and an example of a section layup for the sandwich panel. The layup consists of a face sheet with three top layers and a core material. For each individual layer, three section integration points are used for the *Finite Element Analysis* (FEA).

Table 1: Material properties as specified by the manufacturer.

Engineering constants	*U/D glass*	*Triaxial glass*	*Triaxial glass HRC*	*Biaxial glass*	*Biaxial pre-preg*	*Polymer foam*	*Units*
E_{11}	41.26	20.26	16.70	12.75	11.58	0.0485	GPa
E_{22}	11.39	10.42	8.587	12.75	11.58	0.0485	GPa
ν_{12}	0.33	0.50	0.50	0.50	0.50	0.40	-
G_{12}	3.91	7.35	6.605	10.06	10.06	0.0391	GPa
$\epsilon_{tensile}$	0.021	0.023	0.023	0.017	0.011	-	-
$\epsilon_{compressive}$	0.016	0.012	0.016	0.015	0.014	-	-
ϵ_{shear}	0.0037	0.014	0.014	0.014	0.014	-	-
X^T	903.60	472.06	389.04	214.20	123.91	1.4	MPa
X^C	660.16	324.16	267.15	184.88	156.33	1.3	MPa
Y^T	42.14	127.12	104.76	184.88	156.33	1.4	MPa
Y^C	42.14	127.12	104.76	184.88	156.33	1.3	MPa
S^L	58.65	99.25	89.17	143.91	143.91	1.1	MPa
S^T	58.65	99.25	89.17	143.91	143.91	1.1	MPa
ρ	1931	1864	1683	1894	1890	80	kg/m^3

2.1. Trailing edge modelling strategies

Three different trailing edge modelling approaches were applied, in order demonstrate and compare the appropriateness of different blade modelling approaches. The different trailing edge modelling strategies were applied to the trailing edge region between z=8m to z=34m radial blade position, which represents the trailing edge area where the blade geometry consists of thin, aerodynamically shaped airfoils.

The first trailing edge modelling strategy is a pure shell element model (Figure 2) which represents most of the numerical models used in journal articles, as, for example, in [16, 17].

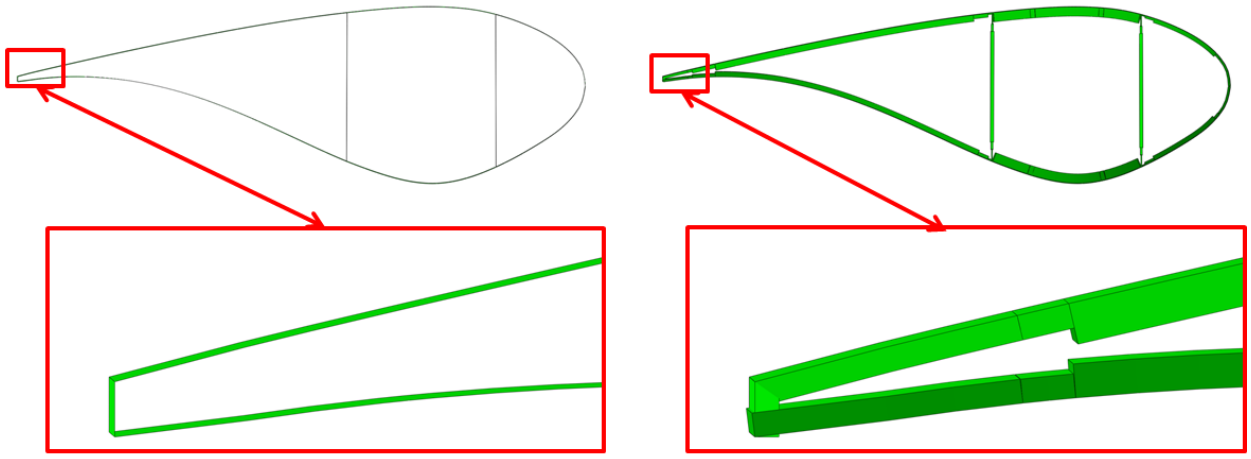

Figure 2: Cross sectional view of the blade. The figure shows the modelling approach of the trailing edge region. The modelling approach used here modelled the trailing edge as a pure-shell modelling approach, where no additional elements and constraints were added. On the left hand side is the shell model, on the right hand side is the shell model which includes the presented shell thickness rendering.

The second trailing edge modelling approach is a shell element model, where the shell elements in the region of the adhesive bondline are constrained via Multi-Point-Constraint (MPC) to each other (Figure 3). The purpose of these MPCs is to tie the region together as the adhesive bondline does in reality. This approach should add more stiffness to the trailing edge region. Two different versions of these modelling approaches were tested, once with a row of elements in the trailing edge, connecting the upper and lower shells, and another time with an open trailing edge between the upper and lower shells. No noticeable differences in the results between both approaches were found.

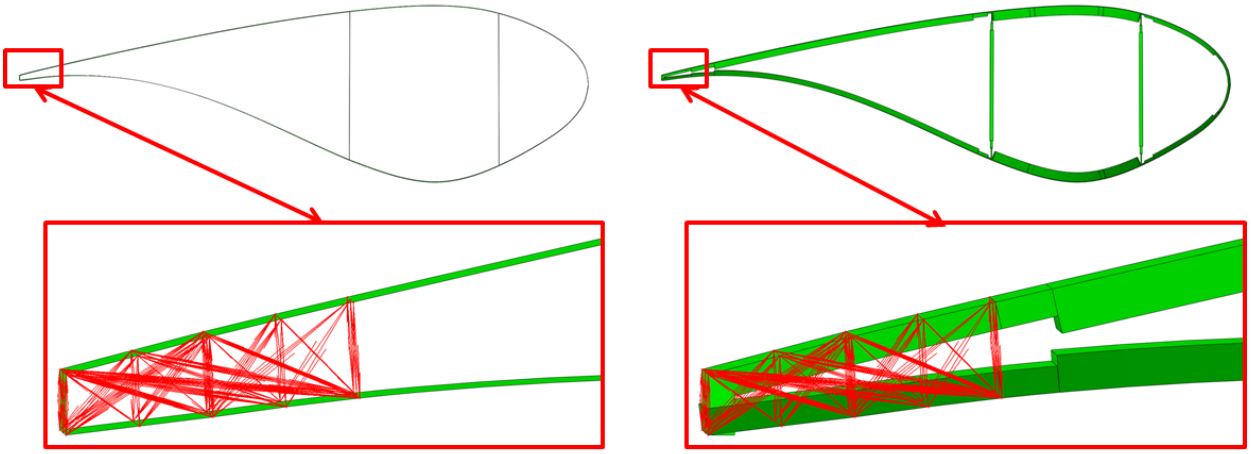

Figure 3: Cross sectional view of the blade. The figure shows the modelling approach of the trailing edge region. The modelling approach used here modelled the trailing edge as a pure-shell modelling approach, but where MPCs were applied to link and stiffen the region. On the left hand side is the shell model, on the right hand side is the shell model which includes the presented shell thickness rendering.

The third trailing edge modelling approach is a combination of shell elements combined with solid elements which represent the adhesive of the trailing edge joint. Here, the solid elements which represent the adhesive bondline are tied together with MPCs to the shell elements discretising the upper and lower panels (Figure 4). The adhesive bondline elements represent a constant bond length of 0.08 m, which was modelled with $3.5x10^4$ 8-node linear brick elements with reduced integration and hourglass control (Abaqus type C3D8I). A convergence study has proven that a characteristic element length of 0.01 m for the 8-node linear brick elements is suitable. The C3D8I elements were connected via tie constraints to the shell elements.

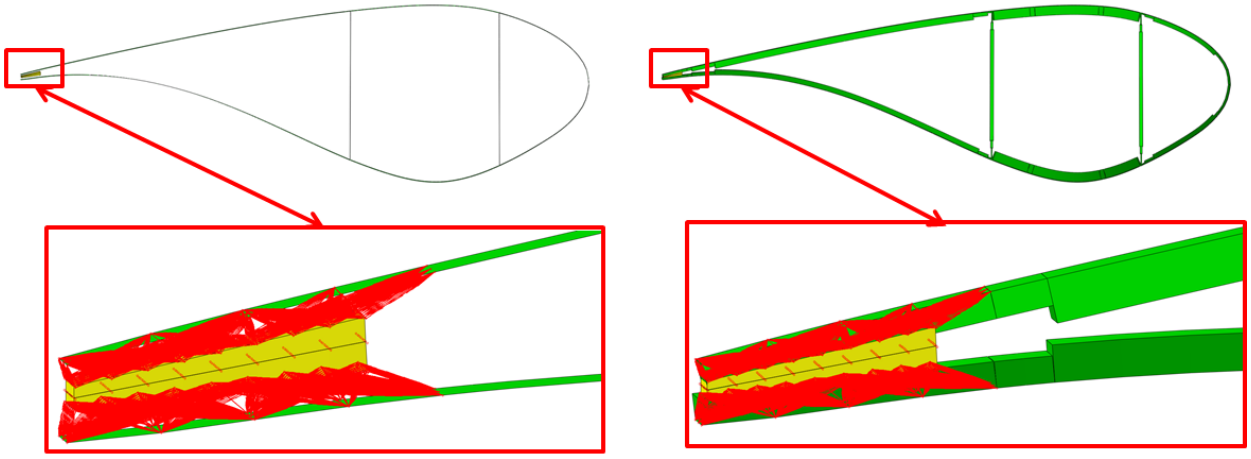

Figure 4: Cross sectional view of the blade. The figure shows the modelling approach of the trailing edge region. The modelling approach used here modelled the trailing edge as a combined shell-solid element modelling approach, where the solid elements were added to the structure which represented the adhesive bondline to link and stiffen the region. On the left hand side is the shell model, on the right hand side is the shell model which includes the presented shell thickness rendering.

2.2. LTT load case

A *Leading edge Towards Trailing edge* (LTT) certification load case was used to test the different modelling strategies. For this purpose, a bending moment distribution matching the certification load for the LTT edge-wise load case was generated by applying five forces in edge-wise direction. The forces were applied to the central master nodes at the aeroelastic centre at cross sections located in the radial blade position of z=13.12m, z=18.61m, z=25.04m, z=30.61 and z=33.09m. From the central nodes, the applied loads were passed on to the upper and lower blade caps via continuum distributing coupling constraints (Figure 5). The surface-based distributed coupling constraints couple the motion of the nodes on the upper and lower blade cap surfaces to the translation and rotation motion of the central master node. The collection of nodes on the caps were constrained to the rigid body motion defined by the central master node (reference node) by allowing control over the transmission of forces through weight factors specified at the coupling nodes [14]. The distributed coupling constraint distributes loads such that the resultants of the forces at the coupling nodes are equivalent to the forces and moments at the reference node [14]. The distributed coupling constraints make it possible to apply forces to the blade without restraining cross-section warping.

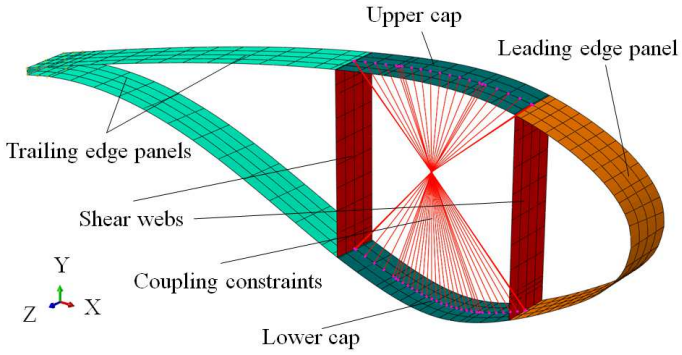

Figure 5: Blade model cross-section slice with the main parts and continuum distributing coupling constraints connected to the shell nodes of the caps with a central master node at the aeroelastic centre (taken from Haselbach et al. [9]).

2.3. Full-scale test

2.3.1. Experimental setup

In order to compare the three different modelling approaches with measurements, data from a full-scale test which had been conducted at DTU Wind Energy on the same blade were used. In the experiments, the blade root was bolted to a test rig with an angle of 8°and under a pitch angle of 120°(Figure 6). The blade was displacement-controlled loaded via four winches which pulled steel cables, connected to anchor plates mounted to the spar cap region of the blade's suction side, through pulleys towards the floor. Thus, the trailing edge experienced a high compressive load due to the applied bending moment in combination with the 120°pitch angle.

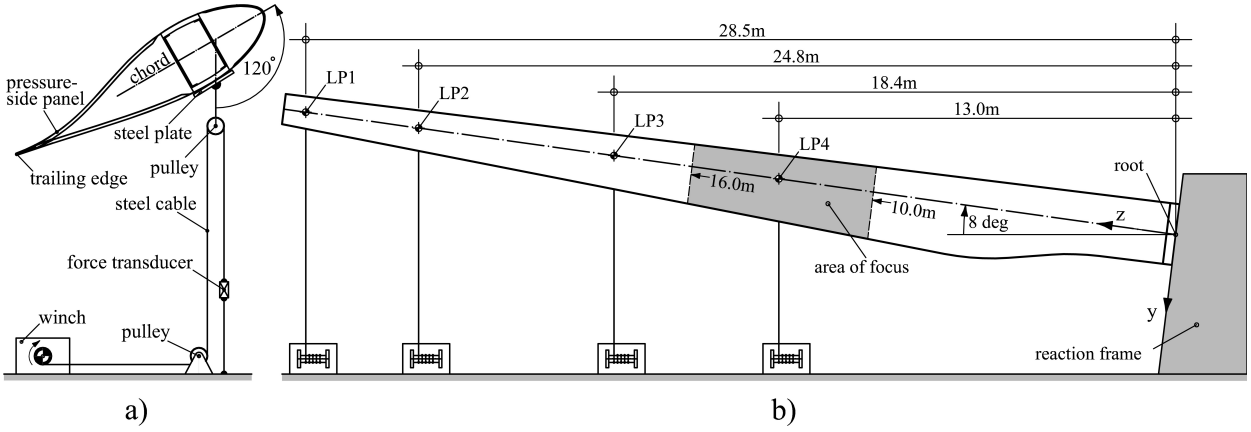

Figure 6: Sketch of the experiment setup (taken from Haselbach et al. [9]).

The blade deflection and was measured by the use of linear cable position sensors, which measured the absolute blade displacement between the suction side cap and floor at four designated radial blade positions (z=10m , z=16m, z=22m and z=29m). Moreover, an optical displacement measurement system based on stereo photogrammetry, which tracked

the relative 3D displacement of marker points along the trailing edge region between 10m and 16m (gray marked area in Figure 6), was used. Longitudinal and transverse surface strains along the adhesive trailing edge joint were measured using fibre-sensing equipment from HBM FiberSensing as well as conventional electrical resistance strain gauges. More details concerning the experiment can be found in the Reference section [9, 18].

2.3.2. Numerical setup

In order to simulate the full-scale test, numerical boundary conditions similar to the experimental setup were applied to the blade model. A kinematic coupling constraint was applied to the nodes of the root section which connected all the nodes to a master node. All six degrees of freedom of the central master node located in the elastic centre were locked. The load introduction points were modelled on four rigid anchor plates positioned on the spar caps on the suction side of the blade which also used kinematic coupling constraints. The loads were applied by axial contraction of connector elements which linked the master points of the kinematic coupled anchor plates to the simulated strong floor of the test facility (Figure 7). Thus, a follower force approach could be realised which corresponded to the experimental setup of the full-scale test. For more information see Reference [9].

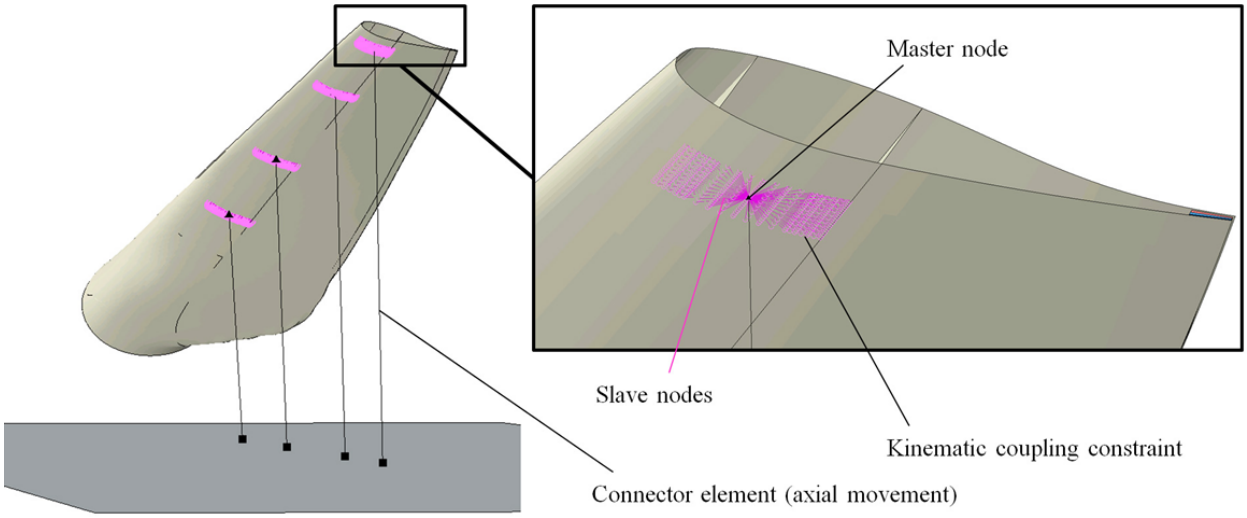

Figure 7: Sketch of the numerical setup (taken from Haselbach et al. [9]).

2.3.3. Computational procedure

The numerical simulations were performed as quasi-static simulations and took geometric nonlinearity into account. Both simulation cases are characterised by high compressive loading of the trailing edge region, and thus geometrical instabilities, referred to as trailing edge buckling, were expected. Trailing edge buckling is defined by a nonlinear increase in out-of-plane deflection, when membrane strain energy converts to bending strain energy [19]. As a consequence, the structural stiffness changes. Mathematically speaking, the transition from stability to instability happens at a critical point, defined as the critical buckling load.

The critical point is characterised with a change in the load-displacement curve.
The standard Newton-Raphson solver is based on a numerical approximation procedure, where the function is approximated by its tangent line. If the function is not continuously differentiable in a neighborhood of the root, then it is very likely that the Newton Raphson solver will always diverge and fail, meaning that the solver cannot find an equilibrium state and convergence is unlikely to happen [20]. In order to overcome these convergence problems, an implicit dynamic solver was chosen for the simulation of the full-scale test case. Here, the loads were linearly ramped up over a period of 10 s so the kinetic energy was at least two orders of magnitude smaller than the strain energy in each time increment. A viscosity coefficient of $1x10^{-4}$ was used to stabilise the numerical simulations.

3. Results

The numerical blade responses of the different trailing edge modelling approaches were compared to each other in an edge-wise certification load case and to the experimental data from the full-scale test. Two different load cases were applied. The first load case represents the blade subject to the certification load case *LTT* (Leading edge Towards Trailing edge), meaning the blade is loaded in an edge-wise direction. The second load case represents the performed full-scale test. Both test cases led to compressive loads in the trailing edge region, and thus were considered as ideal test cases to investigate the trailing edge response for the three different modelling strategies.

3.1. LTT load case

The LTT load case led to high compressive stresses and strains in the trailing edge region. Thus, depending on the trailing edge modelling approaches, different trailing edge responses were predicted. The occurrence of an instability mode in the trailing edge region for the pure shell model terminated the simulation. A load-displacement curve showed that the critical buckling load was reached at this load level. The analyses based on the pure shell model approach did not reach 100% of the LTT load case, it reached the critical buckling load at a load level of 86%; however computations based on the other modelling approaches were completed successfully at 100% load of the LTT certification load case. Slender, flexible structures like trailing edges are prone to show these kind of instabilities, often also referred to as trailing edge buckling. As a consequence of the occurring instability based on highly compressive loads, high strains and stresses at a load level of 86% of the pure shell model were predicted, whereas computations based on the other modelling approaches showed significant lower strains and stresses in the trailing edge region (Figure 8).

The strain plots in Figure 8 clearly indicate the significant differences of the three modelling approaches. Figure 8.1 shows the simulation result of the computations based on the pure shell model approach subjected to 86% of the LTT certification load. Here, the modelling approach predicted an instability which would lead to a wave formation and thus induce critical stresses and strains. Figure 8.2 shows the simulation results of the tied shell model, which converged to 100% of the LTT certification load. No instabilities, wave

formation or significant stress and strain concentrations were visible for this modelling approach. Figure 8.3 shows the simulation results of the combined shell-solid model, which also completed the entire simulation process successfully. Nevertheless, this modelling strategy seemed to predict a slightly more flexible trailing edge configuration.

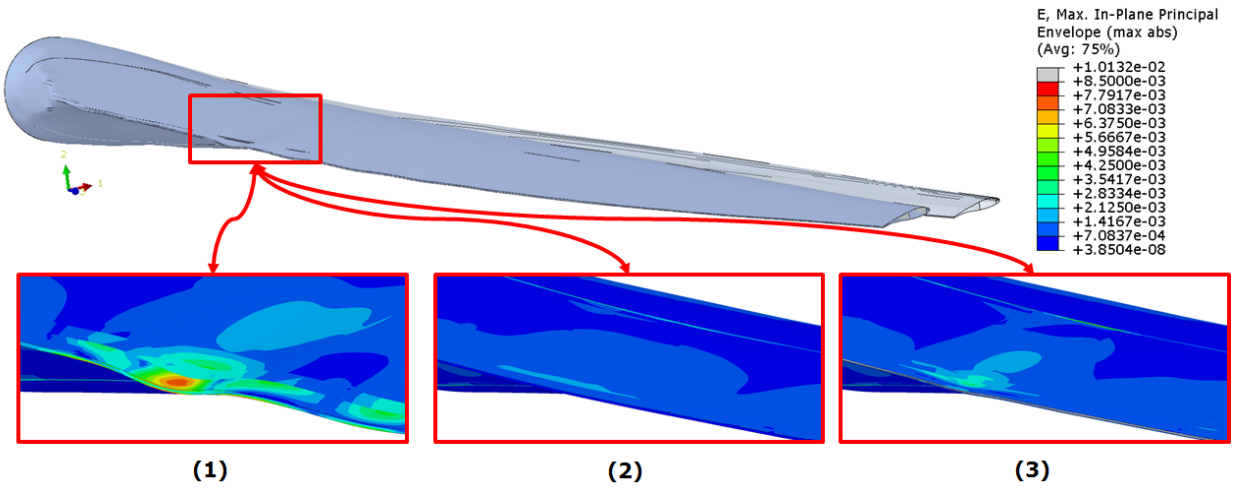

Figure 8: (1) Simulation result of the "pure shell" model subjected to 86% of the LTT certification load. (2) Simulation result of the "tied shell" model subjected to 100% of the LTT certification load. (3) Simulation result of the shell-solid "combined model" subjected to 100% of the LTT certification load.

Figure 9 indicates the results of the Tsai-Wu stress based failure criterion. The failure criterion shows the state of stress relative to the maximum allowable load level defined in a failure envelope. Values of the Tsai-Wu Failure Index (I_F) bigger than one indicate material failure. The failure criterion plots in Figure 9 show similarities to the findings from the strain plots. The simulation results of the pure shell model approach subjected to 86% of the LTT load indicated stress states of between $I_F = 0.5$ to $I_F = 1.0$ in the trailing edge region (9.1). This result would indicate that the blade would have failed or was close to failure. In contrast, the tied shell model showed a failure index of between $I_F = 0.10$ $I_F = 0.25$ at 100% of the LTT load (9.2). The combined shell-solid approach (9.3) showed a more distinct load concentration in the vicinity of the trailing edge than the tied shell model approach, but with lower failure indices compared to the pure shell model. The magnitude of the failure indices is closely linked to instabilities in the trailing edge region, since as soon as an instability appears, stresses and strains, and thus the failure index, increase significantly.

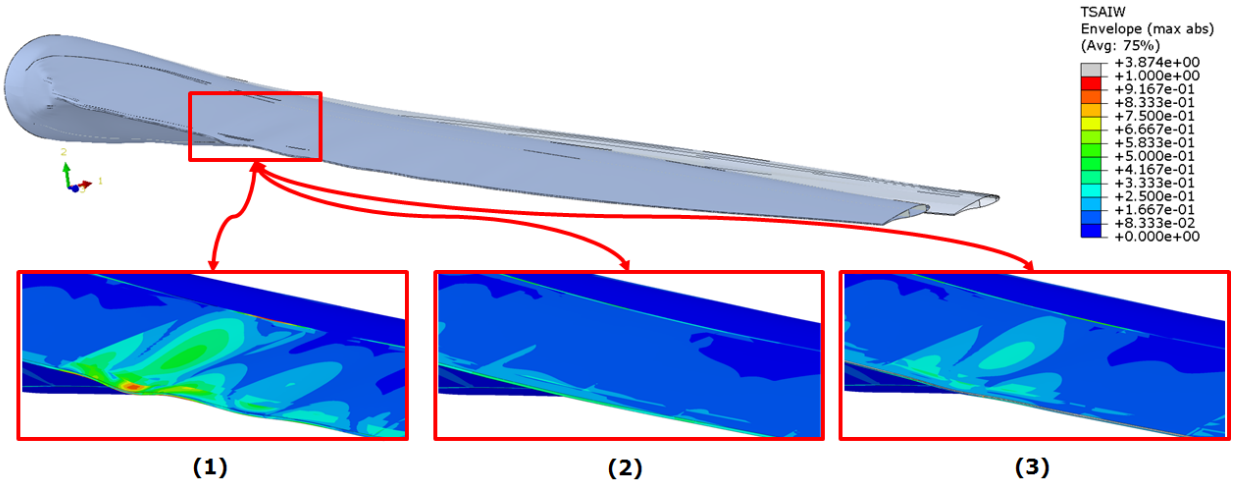

Figure 9: (1) Simulation result of the "pure shell" model subjected to 86% of the LTT certification load. (2) Simulation result of the "tied shell" model subjected to 100% of the LTT certification load. (3) Simulation result of the shell-solid "combined model" subjected to 100% of the LTT certification load.

Figure 10 shows the absolute trailing edge deformation in a y-direction (flap-wise direction) along the blade span for all three modelling approaches. It can clearly be seen that the pure shell model deviates significantly in the prediction of the trailing edge wave magnitudes compared to the other two approaches.

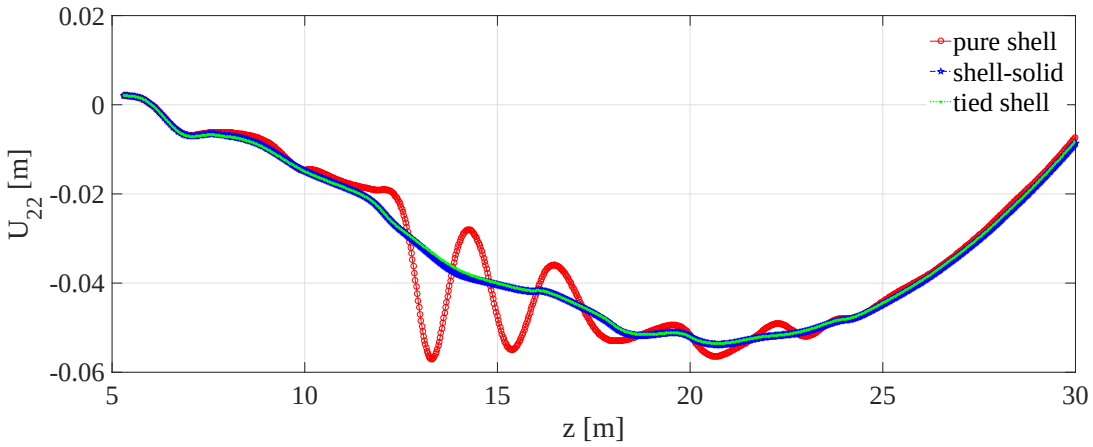

Figure 10: Absolute displacement of the trailing edge in a y-direction plotted over the blade span in a z-direction

3.2. Full-scale test case

In the second numerical study, the three modeling approaches were compared to a full-scale test, as visualized in Figure 11. The advantage of this numerical study was that not only could the different numerical blade models be compared to each other, but the prediction results could also be analysed in respect to the experimental data.

During the test load case, high compressive loads in the trailing edge region occurred, which led to significant instabilities and deformation in the trailing edge region between 12m and 15m. Figure 11 shows the predicted blade deformation just before ultimate blade failure with the distinct wave formation in the trailing edge region. All three models predicted trailing edge deformation, just with partly significant differences of the magnitude and variation of the exact location of the main buckle.

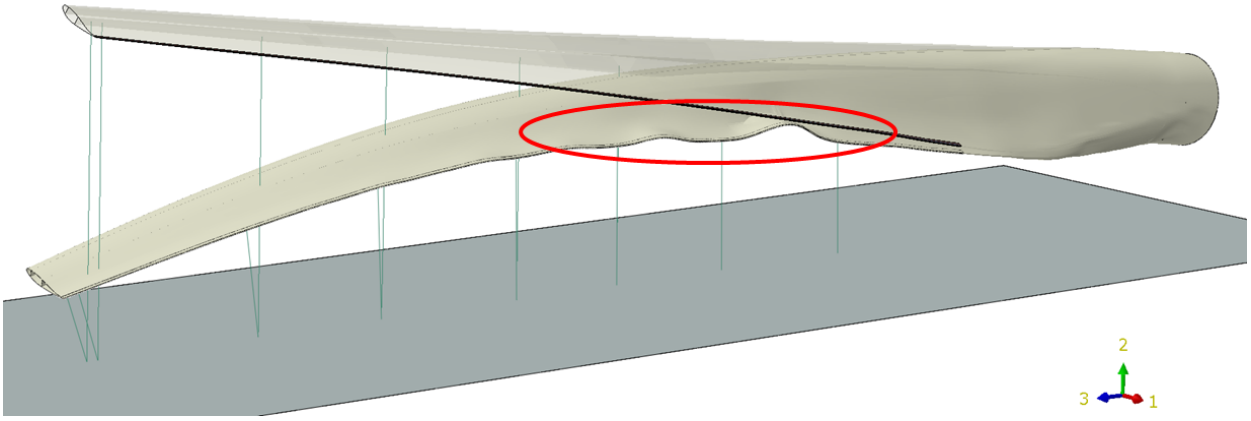

Figure 11: Blade response and trailing edge deformation state just before ultimate blade failure occurred.

The absolute and relative displacements of the trailing edge were compared at a load level of 80%. A load level of 80% was chosen because at this load level, no failure had occurred, whereas for higher load levels, shear core failure in the sandwich material (as reported in [21]) occurred. As a consequence, for load levels above 80%, a change in the structural response occurred, which would have to be included with, for example, progressive damage models, in order to account for a change in the stiffness matrix in the numerical model which considered the stiffness degradation of the sandwich panel in the full-scale test after failure onset, respectively. Thus, at a load level of 80% or below, all effects could be studied without being affected by possible uncertainties caused by failures.

3.2.1. Displacements

Figure 12 shows the absolute displacement in a y-direction (U_{22}) of the trailing edge along the blade span at a load level of approximately 80% for all three numerical models and also for the experiment. From the full scale test, only experimental data measured between z=12.5m and z=16m based on stereo photogrammetry were available. It can clearly be seen that the numerical predicted trailing edge deformation of the pure shell model is significantly more wavy than the predictions of the shell-solid combined modelling approach, the tied shell model and the experimental data.

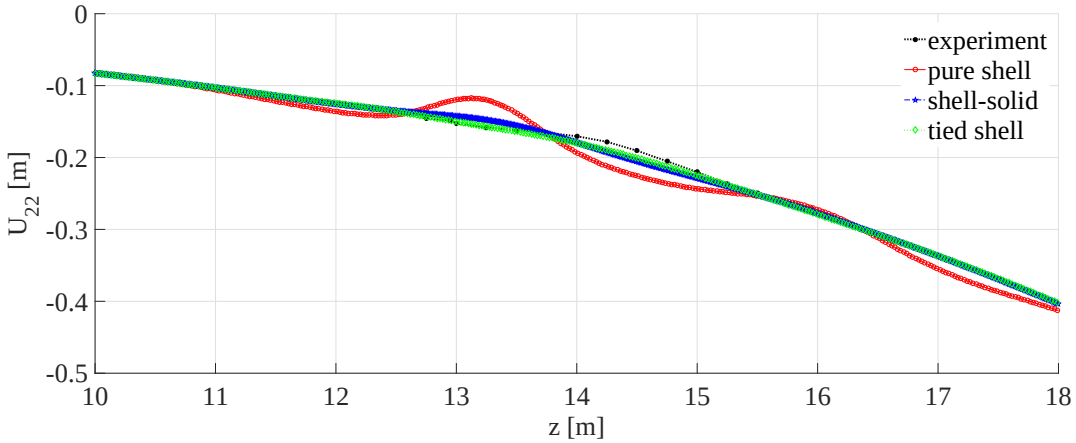

Figure 12: Absolute displacement of the trailing edge (along the blade span) at a load level of approximately 80%.

In order to depict the relative differences and magnitudes of the trailing edge deformation as more visible, the local trailing edge wave deformation was separated from the global deformation. For this purpose, a fifth order polynomial function (Equation 1) was used to represent the numerically obtained global trailing edge deformation. The local difference between the polynomial function and numerical results were calculated, and thus the local wave formation determined. The polynomial function is given in Equation 1

$$u_y(z) = a_0 z^5 + a_1 z^4 + a_2 z^3 + a_3 z^2 + a_4 z + a_5 \tag{1}$$

where the curve fitting constants are a_i and the lengthwise positions measured from the root are represented by z. The fitting constants were obtained in Matlab [22] by a least squares method.

Figure 13 shows the extracted local trailing edge wave formation for all three numerical models and also for the experiment. It can clearly be seen that the pure shell model predicted trailing edge wave formations with much higher magnitudes than were actually experimentally measured in the test. The prediction deviated significantly from the numerical results of the other two blade modelling approaches. While the tied shell model over predicted the trailing edge stiffness, and thus achieved smaller wave formation magnitudes, the shell-solid model predicted the trailing edge wave magnitudes reasonable well. One thing that the models had in common was that they all predicted the position of the local deformation peak with an offset in the z-direction compared to the experimental data.

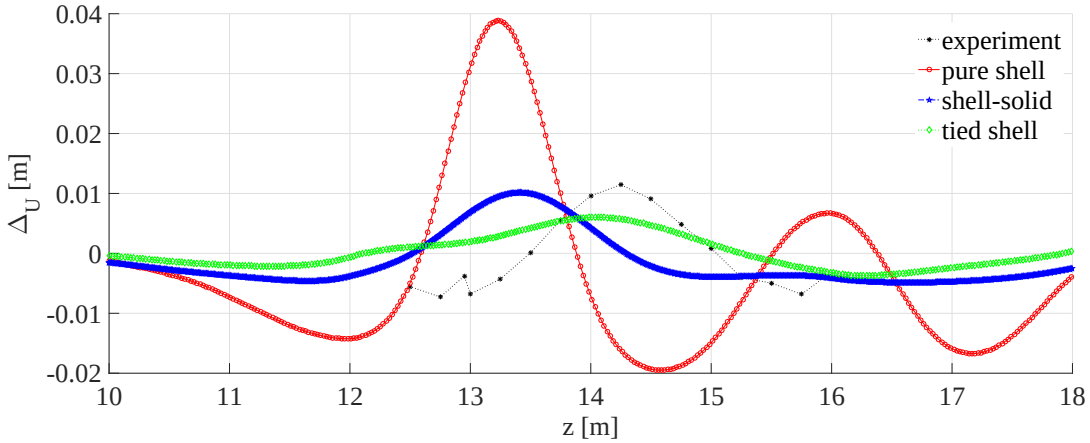

Figure 13: Relative displacement of the trailing edge (along the blade span) at a load level of approximately 80%.

3.2.2. Strains

Beside the displacement predictions, the ability to appropriately predict strain in the trailing edge region is also important for reliable numerical simulations. Here, numerical predictions could be compared to experimentally measured and available strain data in longitudinal and transverse directions at a load level of approximately 57% of the ultimate load.

Figure 14 shows the strain plots in a longitudinal direction. It can clearly be seen that the tied shell model approach and the shell-solid model approach predicted similar longitudinal strains along the blade span, whereas the pure shell model approach differed in the strain prediction. Unfortunately, the experimentally measured longitudinal strain data oscillated extremely, in particular between 10m and 14m, such that a quantity comparison was difficult. The reason for the oscillation is attributable to the placing and measurement of Fibre Bragg Grating (FBG) sensors. Figure 15 shows the effect of FBG strain sensors which were placed in the sandwich core region of the trailing edge panel on the longitudinal strain. The two lines outline the position of the FBG sensors and the transition area between the pure laminate area and the sandwich panel structure. Since the FBG were partly placed on top of the sandwich plane structures, the measurements seemed to be very noisy and thus the magnitudes varied significantly between the adjacent measurement spots. The longitudinal strain measurements showed considerable fluctuations between 10.0m and 14m, whereas the remaining data is more consistent. It was found that the sensors in the noisy area were placed on the sandwich core region of the trailing edge panel, while the remainder were placed on the pure laminate.

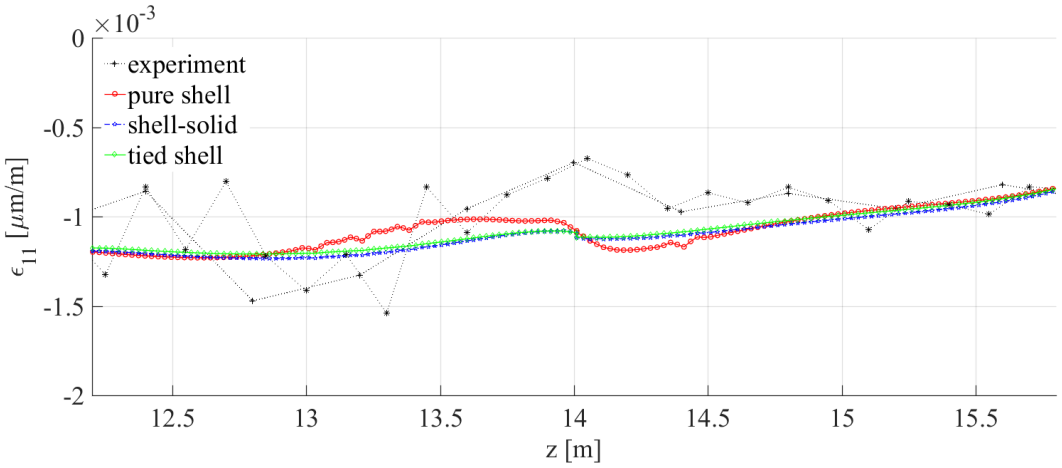

Figure 14: Strain plots in a longitudinal direction (along the blade span) at a load level of 57%.

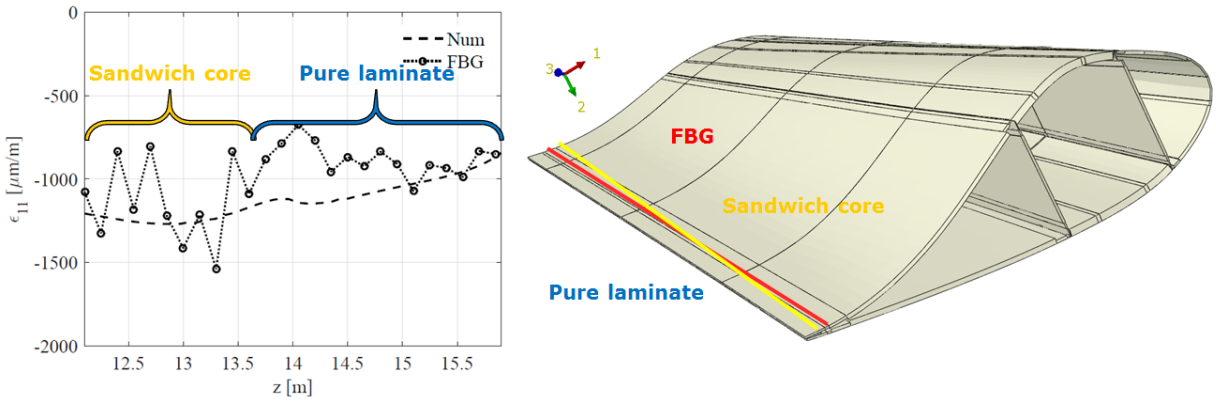

Figure 15: The effect of strain sensors which were placed in the sandwich core region of the trailing edge panel on the longitudinal strain. The two lines outline the position of the Fibre Bragg Grating (FBG) sensors and the transition between the pure laminate area and the sandwich panel structure.

Figure 16 shows the strains in the transverse direction to the blade span. Here, it can clearly be seen that the combined shell-solid modelling approach shows the best agreement compared to the experimental data, whereas the two other approaches predicted strain values which significantly deviated from the measured data.

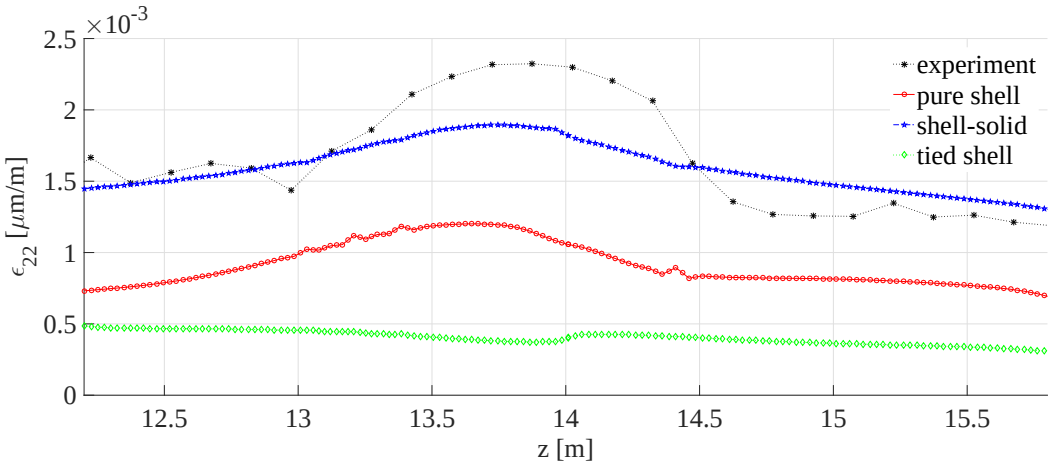

Figure 16: Strain plots in the transverse direction to the blade span at a load level of 57%.

4. Discussion

The study demonstrated the reliability of three different modelling approaches applied to a 34m long wind turbine rotor blade. The meaningfulness of the LTT test case might be limited, since no experimental data were presented. However, the 34m blade series has been in operation since 2003 and has passed the certification scheme – thus no failure in the LTT load case occurred during the static test. In conclusion, the prediction of failures, as seen for the pure shell model for the LTT load case, indicate that the blade response prediction is incorrect. Thus, looking into the LTT test case was justified.

Moreover, by including the LTT load case, two different load cases were presented to compare the different modelling approaches, which makes the study more reliable. A disadvantage of the tests studied in this paper is that only one blade type has been investigated and the results might be slightly different for different blade designs.

However, the presented combined shell-solid trailing edge modelling approach seems to significantly increase the reliability of wind turbine rotor blade shell models. Furthermore, the combined shell-solid modelling approach allows Strain Energy Release Rates (SERR) and/or to simulate failures in the trailing edge to be predicted, since the adhesive bondline can be separated. This advantage allows for the investigation into the effect of adhesive bondline defects in the trailing edge on the blade response as, for example, presented in Haselbach et al. [9, 21].

5. Conclusion

From the presented results of both the LTT simulation and the comparison to the full-scale test, it can be concluded that all three modelling approaches led to deviating results. The pure shell modelling approach, as often used in academia and partly in industry, performed worst compared to the other two modelling approaches used in this study. The pure shell model was not able to predict the trailing edge stiffness correctly. Thus, trailing edge

deformations, stresses and strains, as well as critical load states, in respect to instabilities, were predicted incorrectly. As a consequence, the pure shell model approach cannot be recommended to be used for final design calculation or/and ultimate strength assessments for certification and could lead to more conservative results, making the blade structure heavier than is maybe necessary.

The tied shell modelling approach and the combined shell-solid approach seemed to predict similar displacements, but looking at it in more detail, both approaches showed significant differences not only when looking into the strain and stress fields. Here, the tied shell modelling approach overpredicted the stiffness response of the trailing edge, leading to too little trailing edge deformation and to too small strains and stresses compared to the experimental data. Using the tied shell modelling approach can lead to an underprediction of the real blade performance. In a worse case scenario an overly stiff predicted blade response could lead to damage occurrence and failure in the real blade structure at earlier load levels than expected.

The combined shell-solid modelling approach performed best of all of the three modelling approaches compared to the full-scale test. The results of the comparison between the experimental data and the numerical predictions showed reasonably good agreement in all parts of the results. The demonstrated combined shell-solid modelling approach showed reliable predictions and can be recommended for detailed ultimate strength assessments for wind turbine rotor blades.

6. Acknowledgement

The work is partly supported by the new Danish Centre for Composite Structures and Materials for Wind Turbines (DCCSM), grant no. 09-067212 from the Danish Strategic Research Council. The support is gratefully acknowledged. The work is furthermore partly based on experimental data from a project supported by the Danish Energy Agency through the Energy Technology Development and Demonstration Program (EUDP 2010), grant no. 64011-0006. The supported project is named "Experimental Blade Research Phase 2", and the financial support was greatly appreciated. The author wishes to especially thank Martin A. Eder and Federico Belloni for conducting the blade tests and kindly providing the experimental data.

References

[1] H. Chen, W. Yu, M. Capellaro, A critical assessment of computer tools for calculating composite wind turbine blade properties, Wind Energy 1 (13) (2010) 497–516.

[2] J. P. Blasques, User's Manual for BECAS - A cross section analysis tool for anisotropic and inhomogeneous beam sections of arbitrary geometry, Tech. Rep. Risø-R-1785(EN), Risø DTU, National Laboratory for Sustainable Energy (2011).

[3] HAWC2, HAWC2 - Horizontal Axis Wind turbine simulation Code 2nd generation, `http://www.hawc2.dk`, accessed: 2015-04-24.

[4] L. Damkilde, B. Lund, A Simplified Analysis of the Brazier Effect in Composite Beams, Civil-Comp Press 207 (2009) 1–11.

[5] L. S. Cecchini, P. M. Weaver, Brazier Effect in Multibay Airfoil Sections, AIAA Journal 43 (10) (2005) 2252–2258.
[6] F. M. Jensen, P. M. Weaver, L. S. Cecchini, H. Stang, R. F. Nielsen, The Brazier effect in wind turbine blades and its influence on design, Wind Energy 15 (2012) 319–33.
[7] M. Rosemeier, P. Berring, K. Branner, Non-linear Ultimate Strength and Stability Limit State Analysis of a Wind Turbine Blade, Wind Energy 19 (5) (May 2016) 825–846.
[8] F. M. Jensen, A. S. Puri, J. P. Dear, K. Branner, A. Morris, Investigating the impact of non-linear geometrical effects on wind turbine blades – Part 1: Current status of design and test methods and future challenges in design optimization, Wind Energy 14 (14) (2011) 239–254.
[9] P. U. Haselbach, M. A. Eder, F. Belloni, A comprehensive investigation of trailing edge damage in a wind turbine rotor blade, Wind Energy 19 (2016) 1871–1888, we.1956. doi:10.1002/we.1956.
URL http://dx.doi.org/10.1002/we.1956
[10] M. A. Eder, R. D. Bitsche, A qualitative analytical investigation of geometrically nonlinear effects in wind turbine blade cross sections, Thin-Walled Structures 93 (2015) 1–9.
[11] M. A. Eder, R. D. Bitsche, F. Belloni, Effects of geometric non-linearity on energy release rates in a realistic wind turbine blade cross-section, Composite Structures 132 (15 November 2015) 1075–1084.
[12] F. M. Jensen, B. G. Falzon, J. Ankersen, H. Stang, Structural testing and numerical simulation of a 34 m composite wind turbine blade, Composite Structures 1 (76) (2006) 52–61.
[13] K. Cox, A. Echtermeyer, Structural design and analysis of a 10MW wind turbine blade 24 (1876) (2012) 194–201. doi:10.1016/j.egypro.2012.06.101.
URL http://dx.doi.org/10.1016/j.egypro.2012.06.101
[14] Dassault Systèmes, Abaqus Analysis User's Manual, Vol. 6.14 (2015).
[15] R. D. Bitsche, Modelling of Wind Turbine Blades with Abaqus, Composites Seminar, DTU Risø Campus Roskilde, Denmark, DTU Wind Energy - Technical University of Denmark (2015) 1–14.
URL http://orbit.dtu.dk/files/106681216/Modelling_WTB_ABAQUS_Bitsche.pdf
[16] M. Jureczko, M. Pawlak, A. Mężyk, Optimisation of wind turbine blades, Journal of Materials Processing Technology 1 (167) (2005) 463–471.
[17] M. M. Shokrieh, R. Rafiee, Simulation of fatigue failure in a full composite wind turbine blade, Composite Structures 1 (74) (2005) 332–342.
[18] P. U. Haselbach, K. Branner, Effect of Trailing Edge Damage on Full-Scale Wind Turbine Blade Failure, Proceedings of the 20th International Conference on Composite Materials, Copenhagen.
[19] B. H. Sun, K. Y. Yeh, F. P. J. Rimrott, On the Buckling of Structures, Technische Mecahnik (44) (1995) 129–140.
[20] Wikipedia, Newton's method - Wikipedia, https://de.wikipedia.org/wiki/Newton-Verfahren, accessed: 2017-06-22.
[21] P. U. Haselbach, K. Branner, Initiation of trailing edge failure in full-scale wind turbine blade test, Engineering Fracture Mechanics 162 (2016) 136–154. doi:10.1016/j.engfracmech.2016.04.041.
URL http://www.sciencedirect.com/science/article/pii/S0013794416302065
[22] The MathWorks, Inc., Natick, Massachusetts, United States, MATLAB and Statistics Toolbox Release 2015a (2014).